

Cross section measurements of proton capture reactions relevant to the p process: The case of $^{89}\text{Y}(p, \gamma)^{90}\text{Zr}$ and $^{121,123}\text{Sb}(p, \gamma)^{122,124}\text{Te}$

S. Harissopulos, A. Spyrou,^{*} A. Lagoyannis, M. Axiotis, and P. Demetriou*Institute of Nuclear Physics, National Centre for Scientific Research "Demokritos," POB 60228, 153.10 Aghia Paraskevi, Athens, Greece*J. W. Hammer and R. Kunz[†]*Institut für Strahlenphysik, Universität Stuttgart, Allmandring 3, 70569 Stuttgart, Germany*

H.-W. Becker

DTL/RUBION, Ruhr-Universität Bochum, Universitätsstrasse 150, 40781 Bochum, Germany

(Received 16 June 2012; revised manuscript received 6 January 2013; published 27 February 2013)

The cross sections of the $^{89}\text{Y}(p, \gamma)^{90}\text{Zr}$ and the $^{121,123}\text{Sb}(p, \gamma)^{122,124}\text{Te}$ reactions were determined from γ -angular distribution measurements at beam energies from 1.6 to 3.4 MeV. In addition, angle-integrated cross sections were also measured at $E_p = 2, 3, 4,$ and 4.8 MeV for the $^{89}\text{Y}(p, \gamma)^{90}\text{Zr}$ reaction using the 4π γ -summing method. Astrophysical S factors and reaction rates were deduced from the measured cross sections. Statistical model calculations were performed using the nuclear-reaction code TALYS. The results from the comparison between theory and experiment are discussed in detail.

DOI: [10.1103/PhysRevC.87.025806](https://doi.org/10.1103/PhysRevC.87.025806)

PACS number(s): 24.60.Dr, 25.40.Lw, 26.50.+x, 27.60.+j

I. INTRODUCTION

A very important application of the nuclear reaction theory of Hauser-Feshbach (HF) [1] in nuclear astrophysics is related to the nucleosynthesis processes of the heavier elements. Among these processes, the so-called p process [2] is the nucleosynthetic mechanism of a certain class of 35 proton-rich nuclei known as p nuclei. To explain the observed solar-system p -nuclei abundances that are clear signatures of its creation mechanism, p -process models make use of an extended network of nuclear reactions. This network involves more than 20 000 nuclear reactions on about 2000 nuclei in the mass region from Ni to Bi. Clearly, it is not possible to measure the cross sections of all these reactions, the vast majority of which refer to unstable target nuclei. Therefore, the p -nuclei abundance calculations have to rely largely on the cross section predictions of the HF theory.

In view of this, a validity test of the HF calculations in the mass region of interest would be very useful for the understanding of the existing discrepancies between observed and calculated solar abundances of the p nuclei [2]. Such a test would investigate the uncertainties in the nuclear properties entering the HF calculations, i.e., the nuclear masses, the ground state properties, the nuclear level densities (NLDs) of the involved nuclei, the particle-nucleus optical model potentials (OPs), and finally the γ -ray strength functions. A sensitive check of the reliability and accuracy of the models used to evaluate these nuclear properties requires extensive and detailed comparisons between theoretical predictions and experimental data over a wide mass range. This has motivated

us to perform a systematic study of proton- as well as α -particle-capture reactions involving a series of ≈ 35 cross section measurements in the Cu-Sb region.

As a continuation of our previous communications on these systematics, the present work reports on the results obtained for three of the investigated reactions, i.e., $^{89}\text{Y}(p, \gamma)^{90}\text{Zr}$, $^{121}\text{Sb}(p, \gamma)^{122}\text{Te}$, and $^{123}\text{Sb}(p, \gamma)^{124}\text{Te}$.

II. EXPERIMENTAL PROCEDURES

The cross sections reported here were determined from γ -angular distribution measurements at beam energies ranging from 1.6 to 3.4 MeV. For the $^{89}\text{Y}(p, \gamma)^{90}\text{Zr}$ reaction, angle-integrated cross sections were additionally measured at $E_p = 2, 3, 4,$ and 4.8 MeV by means of the 4π γ -summing method we developed recently [3]. The results presented here for $^{89}\text{Y}(p, \gamma)^{90}\text{Zr}$ are complementary to those we reported in Ref. [4].

A. γ -angular distribution measurements

All γ -angular distribution measurements were carried out at the 4-MV single-ended Dynamitron accelerator operating previously at the University of Stuttgart. The experimental setup used is described in detail in Ref. [5]. It consisted of four large-volume high-purity germanium detectors, all shielded with bismuth germanium oxide (BGO) crystals for Compton background suppression. Three of them had a relative efficiency of $\approx 100\%$, whereas the remaining one had $\approx 76\%$.

The current of the proton beam on the targets varied from 5 to 10 μA . The beam spot had a diameter of ≈ 4 mm. All targets were placed at 90° with respect to the beam axis. They were produced by evaporating natural metallic Y or Sb of high purity (higher than 99.99%) on Ta backings. The latter were 0.2-mm-thick discs with a diameter of ≈ 4 cm. To

^{*}Present address: NCSL, Michigan State University, East Lansing, Michigan 48824, USA.

[†]Present address: DTL/RUBION, Ruhr-Universität Bochum, Universitätsstrasse 150, 40781 Bochum, Germany.

prevent material loss owing to target heating, the backings were cooled directly with water during the whole experiment. The thickness of the targets were determined by means of the x-ray fluorescence (XRF) technique with an accuracy of $\approx 6\%$: the ^{89}Y target was $97 \mu\text{g}/\text{cm}^2$ thick, whereas the $^{\text{nat}}\text{Sb}$ one had a total thickness of $312 \mu\text{g}/\text{cm}^2$. At $E_p = 2 \text{ MeV}$, these thicknesses correspond to ≈ 7 and $\approx 20 \text{ keV}$, respectively. By taking into account the natural abundances of the Sb isotopes, the thickness of the $^{\text{nat}}\text{Sb}$ target results from $178 \mu\text{g}/\text{cm}^2$ of ^{121}Sb and $134 \mu\text{g}/\text{cm}^2$ of ^{123}Sb . All the targets were also checked via the XRF technique for deterioration after the end of the measurements and were found to be stable within 3%.

The detectors were placed on a motor-driven table that could rotate. This way, γ -singles spectra were measured at eight angles with respect to the beam direction. At each angle, two different γ -singles spectra per detector were taken by guiding the corresponding pre-amplifier output signal into two different amplifiers of different gains that further fed two different analog-to-digital converters. Hence, a “low-” and a “high-gain” γ spectrum were obtained from each detector at each angle and beam energy. The former spectrum included γ rays with energies up to $\approx 14 \text{ MeV}$. It was used to obtain the yields of mainly *primary* γ transitions, i.e., γ rays deexciting the so-called *entry* state of the produced nucleus. The high-gain spectrum included γ rays up to $\approx 4 \text{ MeV}$ and was used for the analysis of *secondary* γ transitions, i.e., γ rays deexciting discrete levels below the entry state. The γ -singles spectra were measured at various beam energies ranging from 1.5 to 3.5 MeV. At each energy, additional spectra were taken at each one of the eight angles with the proton beam impinging on a blank backing, to investigate possible yield contributions from reactions occurring in the backing material.

The target-to-detector distances ranged from 10 to 20 cm. Various calibrated radioactive sources (^{60}Co , ^{133}Ba , ^{152}Eu , ^{226}Ra) were used at the end of the runs to determine the absolute efficiency of the setup at all eight angles. In addition, the $^{27}\text{Al}(p, \gamma)^{28}\text{Si}$ reaction was used at the plateau of its 992-keV resonance to obtain γ spectra at all angles. From the latter reaction, relative efficiency curves were determined using the branchings reported by Anttila *et al.* [6], as well as those given in Ref. [7] for γ rays up to $E \approx 12 \text{ MeV}$. The latter relative efficiency curves were then matched to the absolute efficiencies obtained with the sources. These data were furthermore checked for uncertainties owing to coincident summing following the procedure described in Ref. [8]. For this check, an additional ^{57}Co radioactive source was used. As expected, this effect was found to be negligible ($\lesssim 1\%$) because the detectors were placed at sufficiently long distances from the targets.

A typical low-gain γ spectrum measured at $E_p = 3 \text{ MeV}$ for the $^{89}\text{Y}(p, \gamma)^{90}\text{Zr}$ reaction is shown in Fig. 1. In this figure, the primary γ rays are labeled as γ_i , where the integer index i indicates the accession number of the populated excited state of ^{90}Zr according to the level listing of the compilation of Firestone *et al.* [9]. The secondary γ transitions feeding the ground state ($J^\pi = 0^+$) are labeled with their energies followed by a number in brackets indicating the accession number of the deexcited state according to the same level listing. Transitions feeding the first excited state (also a

$J^\pi = 0^+$ level) are marked with “X”. Apart from the γ rays belonging to ^{90}Zr , the spectrum contains also peaks resulting from the $(p, p'\gamma)$ reaction on ^{181}Ta , ^{23}Na , ^{27}Al , ^{19}F , and ^{11}B . The relevant peaks from the first two isotopes are not shown in Fig. 1 as they are located below 0.5 MeV. A careful analysis of the γ spectra taken with the proton beam impinging on the blank Ta backing revealed that the latter contained not only ^{19}F —as normally expected—but also some amounts of ^{23}Na and B. Because of these contaminants, the spectrum shown in Fig. 1 also includes peaks from the reactions $^{27}\text{Al}(p, \gamma)^{28}\text{Si}$, $^{19}\text{F}(p, \gamma)^{20}\text{Ne}$, $^{19}\text{F}(p, \alpha\gamma)^{16}\text{O}$, and $^{11}\text{B}(p, \gamma)^{12}\text{C}$. In addition, one can observe the $2_1^+ \rightarrow 0_1^+$ γ ray of ^{24}Mg (at 1.369 MeV) stemming from $^{23}\text{Na}(p, \gamma)^{24}\text{Mg}$ as well as the γ transition from the direct capture of protons by ^{16}O to the ground state of ^{17}F (peak at 3.424 MeV). The presence of oxygen is attributed to some “light” oxidation of the ^{89}Y target surface. In the spectrum plotted in Fig. 1, three more peaks marked with open circles are shown in the top panel. These are γ rays of unknown origin. They have been, however, observed in many (p, γ) reactions we have investigated so far and are, therefore, taken to be “background” peaks because they were present in our spectra measured independently of the target used. Furthermore, by performing a very detailed check of the level schemes of ^{90}Zr , ^{122}Te , and ^{124}Te in the bibliography we could conclude that none of the other clearly visible peaks, which are unmarked in Fig. 1 or 2, belongs to any of the three nuclei of interest.

It is worth noting that certain primaries have not been observed in the measured spectra, such as, e.g., the γ_3 transition. The absence of these γ rays is attributable either to a very weak intensity or to the large spin difference between the entry and the ground state. As the ground state of the target nucleus ^{89}Y has $J^\pi = 1/2^-$, the spin J of the entry states of the produced ^{90}Zr would most probably have values of $J = 0, 1$, because the relevant proton-beam energies are so low, that they contain only s -wave protons. From this it follows that, the absence of the γ_3 transitions is reasonable, because the third excited state of ^{90}Zr is a $J^\pi = 5^-$ state, and the corresponding primary γ_3 transition would have a spin difference $\Delta I \geq 4$, making it rather unfavorable.

The above arguments also apply, very transparently, to the $^{121}\text{Sb}(p, \gamma)^{122}\text{Te}$ and $^{123}\text{Sb}(p, \gamma)^{124}\text{Te}$ reactions. The target nucleus ^{121}Sb has a ground state with $J^\pi = 5/2^+$, whereas that of ^{123}Sb has $J^\pi = 7/2^+$, leading to entry states of $J = 2, 3$ and $3, 4$, respectively. As a consequence, one expects no γ_0 transition, at least for the $^{123}\text{Sb}(p, \gamma)^{124}\text{Te}$ reaction. Indeed, as can be seen in Fig. 2 no γ_0 transitions have been observed in the γ -singles spectra measured for the $^{\text{nat}}\text{Sb}(p, \gamma)^{122,124}\text{Te}$ reactions. It should be made clear that, parts (c) and (d) of Fig. 2 belong to the same spectrum taken with a “low gain,” as explained above, at $E_p = 3 \text{ MeV}$ and at $\theta = 90^\circ$ to the beam. The black arrows indicate where the γ_0 transitions of the reactions in consideration should appear. Parts (a) and (b) indicate the γ -singles spectrum taken with a “high gain” at the same beam energy and angle.

The absence of γ_0 transitions is not only a feature of the spectra at 3 MeV shown in Fig. 2 but of all the other spectra measured for $^{121}\text{Sb}(p, \gamma)^{122}\text{Te}$ and $^{123}\text{Sb}(p, \gamma)^{124}\text{Te}$. Similarly to the spectrum shown in Fig. 1 for $^{89}\text{Y}(p, \gamma)^{90}\text{Zr}$,

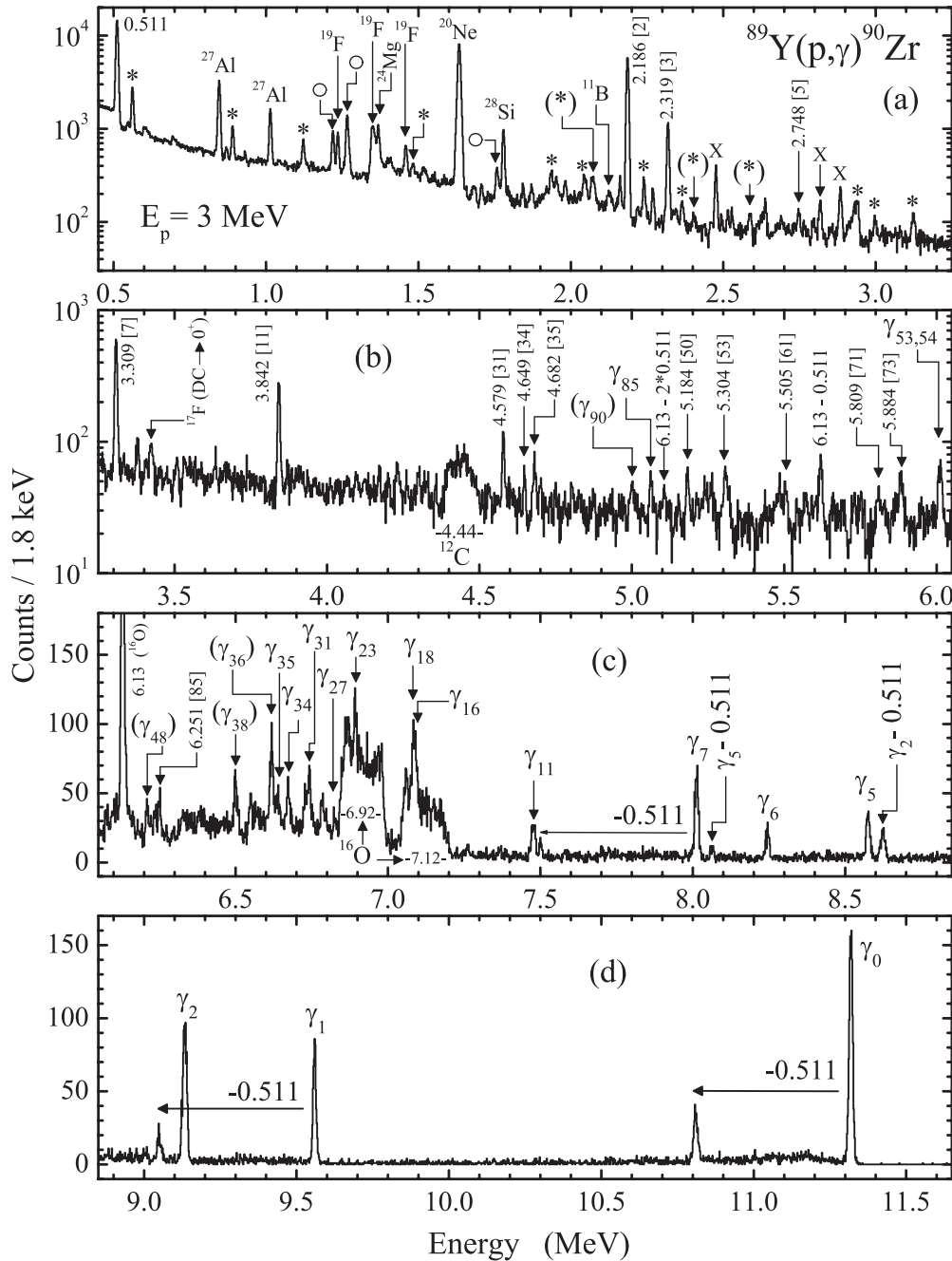


FIG. 1. Typical γ -singles spectrum of the $^{89}\text{Y}(p, \gamma)^{90}\text{Zr}$ reaction taken at $E_p = 3$ MeV and at an angle $\theta = 90^\circ$ to the beam axis. The secondary γ rays feeding the ground state are labeled with numbers corresponding to their energies (in MeV) followed by a number in brackets indicating the level listing according to the compilation of Firestone *et al.* [9]. The primary γ rays are indicated as γ_x , where x is the x th excited state according to the same level listing. Secondary γ transitions between discrete excited states are labeled with a star. Transitions to the first excited ($J^\pi = 0^+$) level are marked with “X”. Parentheses indicate possible assignments. Peaks arising from reactions occurring at the beam collimators (^{27}Al , ^{28}Si) or in the target (^{17}F) and backing material (^{11}B , ^{19}F , ^{12}C , ^{16}O , ^{20}Ne) are explained in the text. Transitions marked with open circles are “background” peaks of unknown origin.

the one plotted in parts (a) and (b) of Fig. 2 contains peaks from $(p, p'\gamma)$ reactions in ^{181}Ta , ^{27}Al , ^{23}Na , ^{19}F , and ^{11}B as well as from (p, γ) and $(p, \alpha\gamma)$ reactions producing ^{28}Si , ^{24}Mg , ^{20}Ne , ^{16}O , and ^{12}C . The peak labeled with ^{137}Cs is the 662-keV γ transition of a ^{137}Cs source used as a “clock” during the measurements with the ^{121}Sb target to check the

dead time. In Fig. 2, there exist peaks marked with “X” or with asterisks, corresponding to γ transitions in ^{121}Sb and ^{123}Sb , respectively, both excited through the $(p, p'\gamma)$ reaction. In addition, the three “background” peaks observed in the $^{89}\text{Y}(p, \gamma)^{90}\text{Zr}$ reaction are also present in parts (a) and (b) of the spectrum. As in Fig. 1, they are marked with open circles.

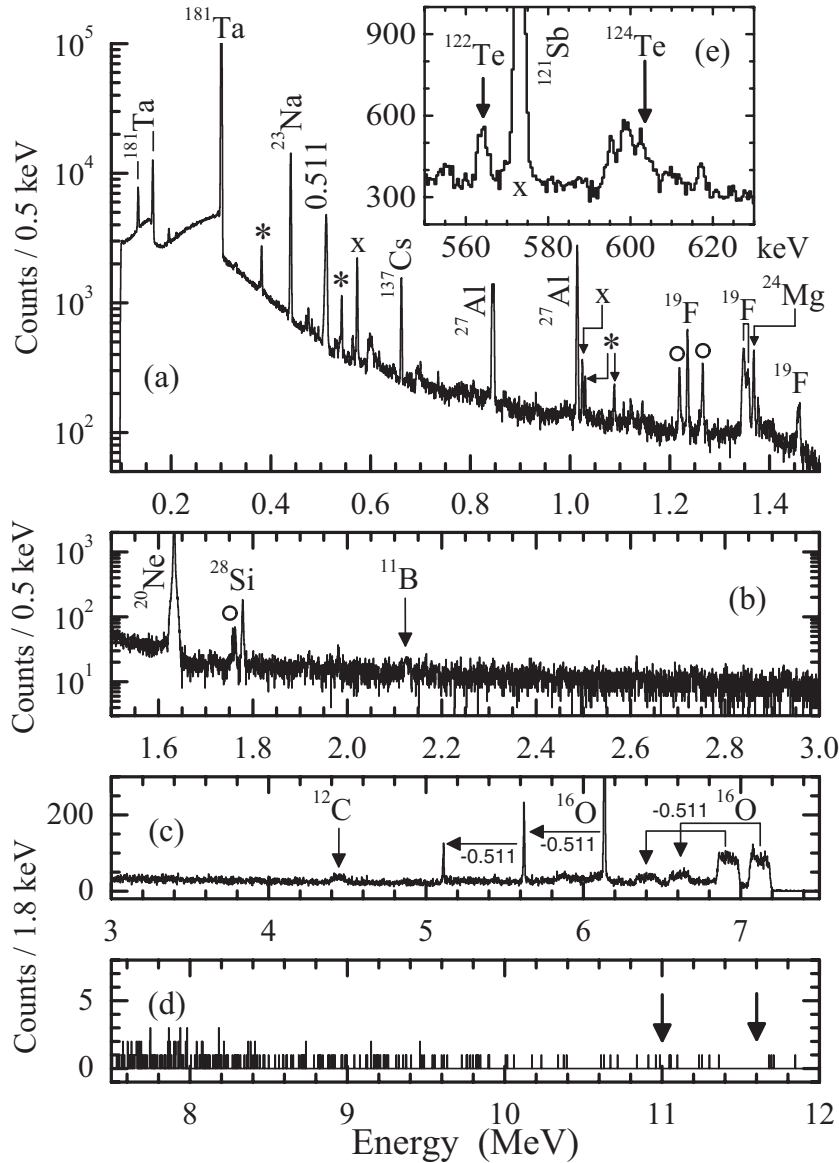


FIG. 2. Typical γ -singles spectra arising from the $^{nat}\text{Sb}(p, \gamma)^{122,124}\text{Te}$ reactions taken at $E_p = 3$ MeV and at an angle $\theta = 90^\circ$ to the beam. Panels (c) and (d) belong to the same spectrum taken with a “low gain” (see in the text). The black arrows indicate where the γ_0 transitions of the reactions in consideration should appear. Panels (a) and (b) indicate the γ -singles spectrum taken with a “high gain.” The peak labeled with ^{137}Cs is the 662-keV γ transition of a ^{137}Cs source used as “clock” during the measurements with the ^{nat}Sb target to check the dead time. Transitions marked with “X” or an asterisk stem from ^{121}Sb and ^{123}Sb , respectively. Peaks arising from reactions occurring at the beam collimators (^{27}Al , ^{28}Si) or in the backing material (^{181}Ta , ^{24}Mg , ^{23}Na , ^{20}Ne , ^{19}F , ^{16}O , ^{12}C , and ^{11}B) are explained in the text. Open circles indicate “background” peaks of unknown origin observed in various (p, γ) measurements of the present systematics.

Finally, panel (e) of Fig. 2 is an enlargement of the 550- to 630-keV range of part (a). The $2_1^+ \rightarrow 0_1^+$ γ transitions resulting from $^{121}\text{Sb}(p, \gamma)^{122}\text{Te}$ and $^{123}\text{Sb}(p, \gamma)^{124}\text{Te}$ are indicated with arrows. It is worth mentioning that in the measured energy range (2.4 to 3.4 MeV), the (p, n) channel is open for both Sb isotopes. As a result, the known “neutron edges” at ≈ 600 and 700 keV are also present in all the measured spectra.

B. Angle-integrated γ -flux measurements

Angle-integrated γ -singles spectra of the $^{89}\text{Y}(p, \gamma)^{90}\text{Zr}$ reaction were measured at beam energies of 2, 3, 4, and 4.8 MeV at the Dynamitron-Tandem-Laboratorium (DTL) of the Ruhr-Universität Bochum, Germany, with the 4π γ -summing technique developed recently [3]. The experimental setup consisted of a 4π single-crystal NaI(Tl) detector (BICRON) of cylindrical shape ($12'' \times 12''$) with a borehole ($\varnothing 35$ mm) along its axis. The target was placed in the borehole

of the detector, at the center of its axis. Thus, the solid angle covered for photons emitted from the target was close to 4π ($\approx 98\%$). The fluorescence light was converted by means of six photomultipliers and the output signals were first gain matched by appropriate high-voltage settings and the resulting sum signal was then fed into a spectroscopic amplifier. The detector had an energy resolution of $\approx 2\%$ at a photon energy of 10 MeV.

The beam current on target ranged from 15 to 25 nA. This way, dead-time effects were kept below 3%. The total accumulated charge ranged from 12 to 30 μC depending on the bombarding energy. The ^{89}Y target had a thickness of $201 \pm 12 \mu\text{g}/\text{cm}^2$. Similarly to the other targets employed in the Stuttgart runs, it was produced by evaporating natural metallic Y of high purity on a Ta backing. Its thickness was determined before and after the cross section measurements by the XRF technique. No significant target deterioration effects were observed.

The 4π γ -summing method employed is based on the use of a large-volume NaI(Tl) detector covering a solid angle

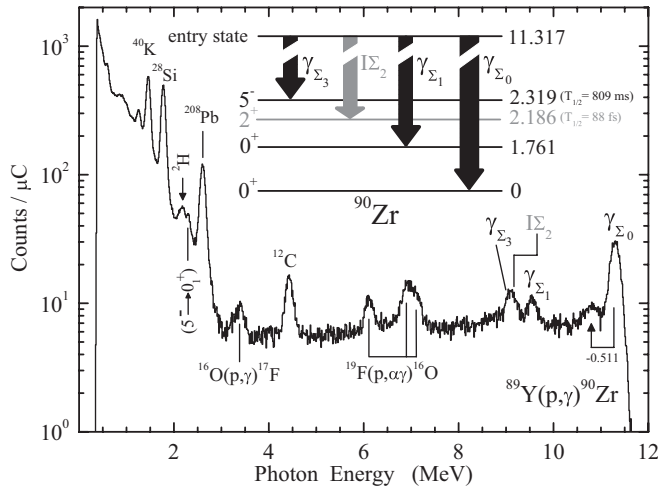


FIG. 3. Typical angle-integrated γ -singles spectrum measured for the $^{89}\text{Y}(p, \gamma)^{90}\text{Zr}$ reaction at $E_p = 3$ MeV with a 4π γ -summing NaI(Tl) detector. The various peaks are explained in the text.

of almost 4π for photons emitted by a target placed at its center. The working principle of such a detector relies on its long time response and its large volume. The latter allows it to fully absorb a photon, whereas the former renders the photomultipliers unable to distinguish between different photons emitted within a time interval smaller than the decay time of the crystal, which is typically $\lesssim 250$ ns. As a result, the corresponding photons are recognized as one photon with an energy equal to the sum of their individual energies and a prominent peak appears in the measured γ spectra at an energy $E_\Sigma = Q + E_{c.m.}$, where Q is the Q value of the reaction and $E_{c.m.}$ is the center-of-mass energy. Owing to the 4π geometry covered by the summing crystal, the observed γ -ray fluxes are angle integrated and systematic errors owing to γ -angular distribution effects are eliminated. Moreover, instead of measuring a large number of γ -angular distributions and further analyzing numerous γ transitions, one needs to acquire only one spectrum and analyze only the sum peak. The 4π γ -summing method has recently been used successfully to determine cross sections of (p, γ) reactions in Pd isotopes [10].

A typical angle-integrated γ -singles spectrum measured at $E_p = 3$ MeV for the $^{89}\text{Y}(p, \gamma)^{90}\text{Zr}$ reaction is shown in Fig. 3. As expected, the spectrum includes the known natural background lines at 1.461, 2.2, and 2.614 MeV, as well as peaks from reactions of the proton beam with ^{27}Al , ^{19}F , ^{16}O , and ^{11}B , which have already been explained in the former section.

As can be observed, the spectrum does not consist of just a single peak, as ideally expected, but of many other peaks as well as a Compton continuum. The latter arises because some photons are not fully absorbed. In particular, the spectrum shown in Fig. 3 includes three sum peaks, labeled as γ_{Σ_0} , γ_{Σ_1} , and γ_{Σ_3} . The first one is located at 11.317 MeV, whereas the other two appear at lower energies differing by ≈ 1.761 and 2.319 MeV from the first one, and they all belong to ^{90}Zr . The first sum peak (γ_{Σ_0}) is the result of the sum of the γ_0 transition from the entry state and all the γ cascades that bypass the first excited level and feed the ground state, as shown in the inset of Fig. 3. The γ_{Σ_1} transition is the sum of all cascades

starting from the entry state and feeding the first excited state at 1.761 MeV, which as a $J^\pi = 0^+$ state decays to the ground state via an $E0$ transition. Finally, the γ_{Σ_3} transition results from summing all γ cascades arriving at the third excited state at 2.319 MeV with $J^\pi = 5^-$. The latter state has a half-life of 809 ms that is considerably longer than the decay time of the NaI(Tl) crystal. As a result, the associated cascading transitions form an independent sum peak and the subsequent “delayed” $5^- \rightarrow 0_1^+$ transition arises in the spectrum as an individual peak. In addition to the three aforementioned sum peaks γ_{Σ_0} , γ_{Σ_1} , and γ_{Σ_3} , the spectrum plotted in Fig. 3 contains a fourth peak at ≈ 9.13 MeV labeled as $1\Sigma_2$ that, owing to the poor resolution of the NaI(Tl) detector, cannot be resolved from γ_{Σ_3} . $1\Sigma_2$ is the result of the incomplete summing; i.e., some portion of the 2186-keV photons emitted by ^{90}Zr are not summed by the detector with the γ cascades feeding into the second excited level that they deexcite. As a result, one observes a peak at energy smaller by 2186 keV from γ_{Σ_0} . The gray arrow in the inset of Fig. 3 indicates the summed γ cascades that result in $1\Sigma_2$, although the half-life of the 2186-keV excited level is very short.

It is worth emphasizing that the effect of incomplete summing of a γ transition appears the stronger, the stronger is the intensity of the transition involved. This has already been observed and discussed in detail in our previous work [11] on the $^{27}\text{Al}(p, \gamma)^{28}\text{Si}$ reaction, where the same detector was employed. Similarly to that case, almost 50% of the photons emitted by the $^{89}\text{Y}(p, \gamma)^{90}\text{Zr}$ reaction studied in the present work depopulate the $J^\pi = 2^+$ excited state at 2186 keV and populate the ground state of ^{90}Zr .

III. DATA ANALYSIS AND RESULTS

The total cross section σ_T of a capture reaction is derived from the total reaction yield Y using

$$\sigma_T = \frac{A}{N_A} \frac{Y}{\xi}, \quad (1)$$

where A is the atomic weight of the target used in amu, N_A is the Avogadro number, and ξ is the target thickness. Depending on the experimental approach used, the total reaction yield Y is derived either from the absolute γ -angular distributions of all the *primary* γ transitions or from the absolute intensity of the sum peak when the 4π γ -summing method is employed.

In the former case, the total reaction yield Y is deduced from

$$Y = \sum_i^N A_0^i, \quad (2)$$

where N is the total number of the γ transitions involved and A_0 the known (absolute) coefficients of the corresponding angular distributions $I(\theta, \varepsilon, N_b)$. The angular distributions consist of data points that are corrected for the (absolute) efficiency ε and the corresponding number N_b of the incoming beam particles. N_b is determined by measuring the beam current and further integrating it over the measurement time by means of a current integrator. The angular distribution of each γ transition is fitted by a sum of Legendre polynomials

$P_k(\theta)$ of the form

$$W(\theta) = A_0 \left[1 + \sum_k a_k P_k(\theta) \right], \quad (3)$$

to determine the well-known energy-dependent coefficients A_0 and a_k ($k = 2, \dots$). In practice, the total cross section is determined from the angular distributions of the γ transitions feeding the ground state and not from those of the primary γ rays. This procedure is followed not only to take advantage of the higher efficiency of the detector for the former γ rays but also to avoid errors owing to the particle decay of the compound nucleus as well as systematic errors owing to uncertainties in the level scheme at high excitation energies.

A crucial point in this method is the determination of the absolute A_0 coefficient of the γ_0 transition, i.e., the γ -ray depopulating the entry level and feeding directly the ground state. This transition often has an energy exceeding 10 MeV and, thus, it is difficult to extract its angular distribution without employing a very efficient setup such as those used in the present work. The intensity of the γ_0 transition can, in principle, be a negligible fraction of the total reaction yield, but this cannot be assumed *a priori*. The same holds for any primary γ ray feeding an excited level that is depopulated by an $E0$ transition. In our case, this applies to the γ_1 transition feeding the first excited state of ^{90}Zr at an excitation energy of 1761 keV.

From Eq. (2) it is obvious that determining cross sections from γ -angular distribution measurements can become very time consuming with increasing number N of the γ transitions. This is clearly demonstrated in the case of the $^{89}\text{Y}(p, \gamma)^{90}\text{Zr}$ reaction: The analysis of the spectra measured at $E_p = 3$ MeV revealed a complex decay scheme for ^{90}Zr , which is shown in Fig. 4. According to this, there exist 15 γ transitions feeding the ground state. In addition to these, there are four more γ rays feeding the first excited level which is deexcited to the ground state via an $E0$ transition; i.e., it is not depopulated via γ rays. The latter four γ transitions need to be taken into account in Eq. (2). As a result, the cross section of $^{89}\text{Y}(p, \gamma)^{90}\text{Zr}$ at 3 MeV was obtained by applying Eq. (2) for $N = 19$ γ transitions which are indicated with black arrows in Fig. 4. The cross sections at the remaining measured energies were derived similarly.

In contrast to the complex picture described above, the situation becomes simpler when all capture events are “gathered” in only one excited level, i.e., when the relevant γ cascades feed only one state, most likely the first excited state, which then deexcites to the ground state by a single γ transition, as was reported in Ref. [12]. The analysis of the spectra measured for the $^{121,123}\text{Sb}(p, \gamma)^{122,124}\text{Te}$ reactions showed something similar. All capture events proceed via the corresponding γ transitions depopulating the first excited states in the produced nuclei; therefore, only the corresponding $2_1^+ \rightarrow 0_1^+$ γ transitions needed to be analyzed.

Typical angular distributions of some of the relevant γ transitions in ^{90}Zr are shown in Fig. 5. For the 564 and 603 keV $2_1^+ \rightarrow 0_1^+$ γ transitions of ^{122}Te and ^{124}Te , respectively, no significant angular effects were found. As shown in Fig. 6, these transitions were almost isotropic. The analysis

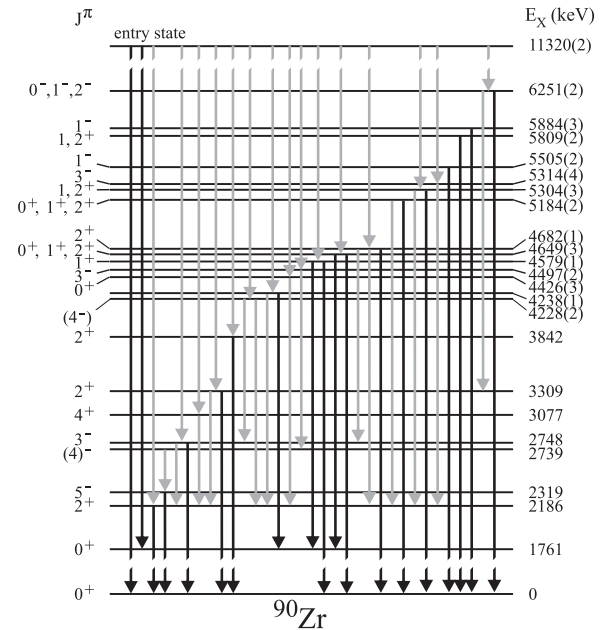


FIG. 4. Decay scheme of ^{90}Zr observed in the present work at $E_p = 3$ MeV. The γ transitions taken into account to determine the cross section of the $^{89}\text{Y}(p, \gamma)^{90}\text{Zr}$ reaction are indicated with black arrows (see also text).

of the angular distributions gave for each γ transition the corresponding “absolute” A_0 coefficient. The influence of solid angle effects were investigated following the procedure described in Ref. [13] and the resulting uncertainties in the A_0 coefficients were found to be of the order of $\lesssim 3\%$.

When the 4π γ -summing method [3,10] is employed, Eq. (2) is replaced with

$$Y = \frac{I_\Sigma}{N_b \varepsilon_\Sigma}, \quad (4)$$

where I_Σ is the intensity of the sum peak, N_b is the number of the beam particles, and ε_Σ is the sum-peak efficiency. The latter quantity depends strongly on the multiplicities of the γ cascades involved and, as such, is in most cases unknown. For this reason, we developed a new method to determine first the average multiplicities of the γ cascades “summed” by our detector and then the corresponding sum-peak efficiency ε_Σ using the GEANT4 Monte Carlo code [14]. This method is explained in detail in Refs. [3,10] and is, therefore, not presented here. The application of this method to $^{89}\text{Y}(p, \gamma)^{90}\text{Zr}$ yielded absolute efficiencies from $32.5\% \pm 3\%$ to $8.5\% \pm 1.0\%$ for sum-peak energies between 8.0 and 13.1 MeV, respectively.

For the three sum peaks labeled γ_{Σ_0} , γ_{Σ_1} , and γ_{Σ_3} observed in the angle-integrated γ spectra for $^{89}\text{Y}(p, \gamma)^{90}\text{Zr}$, the corresponding yields Y_{Σ_0} , Y_{Σ_1} , and Y_{Σ_3} were derived using Eq. (4) and the total reaction yield Y was deduced from their sum, i.e.,

$$Y = Y_{\Sigma_0} + Y_{\Sigma_1} + Y_{\Sigma_3}, \quad (5)$$

which was then inserted into Eq. (1) to give the total cross section. It is worth emphasizing here that the I_{Σ_2} peak arising from incomplete summing is *correctly* not included in Eq. (5).

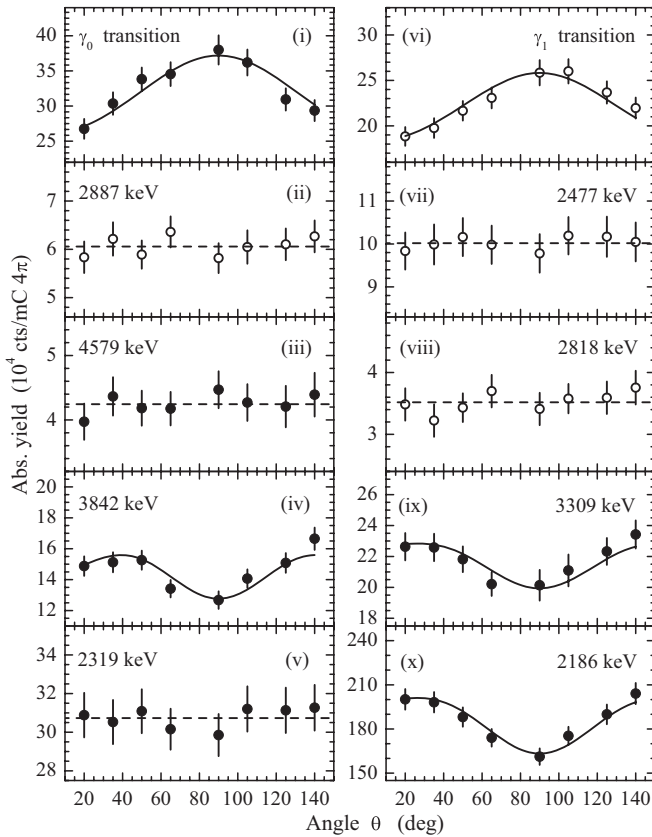


FIG. 5. Some typical angular distributions of γ transitions depopulating excited levels in the ^{90}Zr nucleus. The primaries from the entry level to the ground and first excited states, γ_0 and γ_1 , respectively, are shown in the upper parts of the figure. Angular distributions plotted with open circles belong to γ rays feeding the first excited state, whereas those shown with filled ones to γ transitions populating the ground state (see also text).

This is because, the 4π γ -summing method presented in Ref. [3] is not affected by incomplete summing effects as the sum-peak efficiency ε_{Σ} entering Eq. (4) refers to complete summing only. Hence, our cross section results do not suffer from systematic errors because $1/\Sigma_2$ is not entering Eq. (5).

The results of the cross sections derived in the present work are given in Tables I–III for the reactions $^{89}\text{Y}(p, \gamma)^{90}\text{Zr}$, $^{121}\text{Sb}(p, \gamma)^{122}\text{Te}$, and $^{123}\text{Sb}(p, \gamma)^{124}\text{Te}$, respectively. In the case of the γ -angular distribution measurements (first 19 rows of Table I and data in Tables II and III), the associated errors in the measured cross sections range from 3.5% to 35%, depending on the beam energy. The major contribution to errors that are smaller than 8% comes from the uncertainties in the target thickness ($\approx 6\%$), accumulated charge ($\approx 3\%$) and detector efficiency ($\approx 2\text{--}3\%$), because the corresponding statistical errors are below 2%. The latter were considerably higher, i.e., between 10% and 35%, in all cases with relative cross section errors larger than 8%.

In the case of the angle-integrated measurements performed at Bochum, i.e., the four data points listed in rows 20 to 23 of Table I, the uncertainties owing to target-thickness and accumulated charge were the same and the statistical errors ranged between 2% and 7%. The major contribution

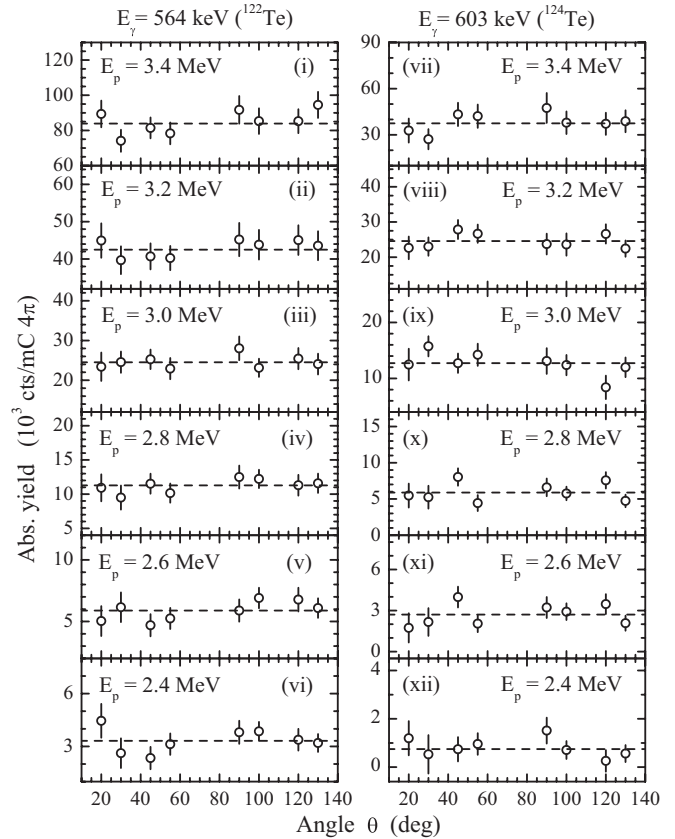


FIG. 6. Angular distributions of the $2_1^+ \rightarrow 0_1^+$ γ transitions of the ^{122}Te (left panels) and ^{124}Te (right panels) measured in the present work. The corresponding proton-beam energies E_p are also indicated.

to the given errors in the cross section comes from the uncertainties in the sum-peak efficiency; for γ_{Σ_0} , the absolute sum-peak efficiency was 8.6% at $E_{c.m.} = 4.743$ and 13.7% at $E_{c.m.} = 1.973$. The corresponding efficiencies for γ_{Σ_1} were 10.8% and 25.4% and for γ_{Σ_3} they were 12.2% and 32.5%, respectively. The relative error for all sum-peak efficiencies was ranging between 9% and 12%.

The center-of-mass energies given in the first column of Tables I–III are the effective beam energies E_{eff} in the center-of-mass system obtained from

$$E_{\text{eff}} = E_p - \frac{\Delta E}{2}, \quad (6)$$

where E_p is the proton-beam energy and ΔE is the corresponding target thickness that was determined using appropriate stopping powers [15].

The cross sections presented in Tables I–III have been corrected for electron-screening effects [16,17]. The latter were found to result in an increase of the cross section by up to $\approx 12\%$. This enhancement was obtained by applying an electron screening factor f given by [18]

$$f(E) = \frac{E}{E + U_S} \times \exp\left[\frac{\pi\eta(E) \times U_S}{E}\right], \quad (7)$$

where U_S is the screening potential obtained from appropriate charge scaling [18] of the typical screening energy value of ≈ 300 eV observed for the $d + d$ fusion reaction in metals

TABLE I. Total cross sections σ_T and astrophysical S factors determined in the present work for the $^{89}\text{Y}(p, \gamma)^{90}\text{Zr}$ reaction from γ -angular distribution measurements (first 19 rows, from $E_{\text{c.m.}} = 1.588$ to 3.383 MeV) and from angle-integrated γ -flux measurements (next 4 rows, from $E_{\text{c.m.}} = 1.973$ to 4.743 MeV). The data of our earlier work [4] are also included (last 13 rows). The effective energy in the center-of-mass system is given in the 1st column. The corresponding error does not exceed 10 keV. The σ_T (2nd column) as well as the S factor (3rd column) are corrected for electron screening effects as described in Sec. III. The corresponding screening factors f_s are given in the last column. They were calculated using Eq. (7).

$E_{\text{c.m.}}$ (MeV)	σ_T (μb)	S factor (10^3 MeV b)	f_s
1.588	1.8 ± 0.5	$54\,030 \pm 15\,010$	1.111
1.689	3.5 ± 0.6	$44\,170 \pm 7572$	1.100
1.788	5.8 ± 0.7	$33\,710 \pm 4069$	1.092
1.888	9.9 ± 0.9	$28\,040 \pm 2549$	1.084
1.988	23.7 ± 1.5	$34\,600 \pm 2190$	1.077
2.088	35.0 ± 1.6	$27\,670 \pm 1265$	1.072
2.188	52.4 ± 2.4	$23\,440 \pm 1074$	1.066
2.287	85.3 ± 3.9	$22\,560 \pm 1031$	1.062
2.387	139 ± 6	$22\,370 \pm 966$	1.058
2.487	182 ± 8	$18\,390 \pm 809$	1.054
2.587	245 ± 9	$15\,990 \pm 587$	1.051
2.687	328 ± 12	$14\,180 \pm 519$	1.048
2.786	358 ± 12	$10\,530 \pm 353$	1.045
2.864	450 ± 15	9914 ± 331	1.043
2.986	599 ± 20	8600 ± 287	1.041
3.086	868 ± 29	8948 ± 299	1.039
3.186	1037 ± 34	7802 ± 256	1.037
3.286	1394 ± 45	7769 ± 251	1.035
3.383	1489 ± 49	6286 ± 207	1.033
1.973	19 ± 3	$30\,540 \pm 4822$	1.078
2.962	659 ± 96	$10\,270 \pm 1496$	1.051
3.952	2614 ± 356	2692 ± 367	1.026
4.743	2048 ± 293	467 ± 67	1.020
1.757	7.3 ± 1.8	$53\,700 \pm 13\,240$	1.094
1.961	24.1 ± 4.6	$41\,860 \pm 7990$	1.079
2.160	37.5 ± 5.6	$19\,600 \pm 2926$	1.068
2.359	111 ± 15	$20\,460 \pm 2765$	1.059
2.656	323 ± 40	$15\,820 \pm 1960$	1.049
2.953	676 ± 83	$10\,870 \pm 1334$	1.041
3.250	1305 ± 145	8089 ± 899	1.035
3.448	1843 ± 203	6503 ± 716	1.032
3.843	2619 ± 288	3445 ± 379	1.027
4.140	2867 ± 287	1982 ± 198	1.024
4.437	2233 ± 225	868 ± 87	1.022
4.635	2085 ± 188	571 ± 51	1.020
4.832	2112 ± 191	417 ± 38	1.019

[17,18], E is the center-of-mass energy, and η is the Sommerfeld parameter [16] defined by

$$2\pi\eta = 31.29 \times Z_1 \times Z_2 \times \left(\frac{\mu}{E}\right)^{1/2}. \quad (8)$$

In the case of ^{89}Y the charge-scaled screening potential $U_S = 11.7$ keV, whereas for ^{121}Sb and ^{123}Sb $U_S = 15.3$ keV. The values of the screening-correction factor f for the

TABLE II. Total cross sections σ_T and astrophysical S factors determined in the present work for the $^{121}\text{Sb}(p, \gamma)^{122}\text{Te}$ reaction from γ -angular distribution measurements. The effective energy in the center-of-mass system is given in the first column. Its error is less than 10 keV. The σ_T (second column) as well as the S factor (third column) are corrected for electron screening effects as described in Sec. III. The corresponding screening factors f_s are given in the last column. They were calculated using Eq. (7).

$E_{\text{c.m.}}$ (MeV)	σ_T (μb)	S factor (10^3 MeV b)	f_s
2.383	0.6 ± 0.1	$223\,400 \pm 37\,230$	1.104
2.583	1.2 ± 0.1	$133\,200 \pm 11\,100$	1.091
2.783	2.5 ± 0.2	$94\,770 \pm 7581$	1.081
2.983	4.9 ± 0.3	$70\,980 \pm 4345$	1.072
3.183	8.7 ± 0.4	$52\,920 \pm 2433$	1.065
3.383	17.1 ± 0.7	$47\,310 \pm 1937$	1.059

reactions under investigation are given in Tables I–III together with the electron-screening-corrected astrophysical S factors. The latter were determined from the electron-screening-corrected cross sections σ_T using

$$S(E) = \sigma_{T(E)} E e^{2\pi\eta(E)}. \quad (9)$$

To demonstrate the agreement between the results we obtained from the γ -angular distributions and the 4π γ -summing method, we compare the total as well as some “partial” screening-corrected cross sections in Fig. 7. In the top panel (a), the screening-corrected total cross sections σ_T determined from the γ -angular distribution measurements (open circles) are plotted together with the screening-corrected data we reported in Ref. [4] (open squares) and those obtained in the present work using the 4π γ -summing technique (solid circles). In the middle panel (b), we compare the sum of the screening-corrected cross sections derived from the angular distributions of all the γ transitions feeding the first (0^+) excited state in ^{90}Zr with the corresponding ones derived from the sum peak γ_{Σ_1} . The screening-corrected cross section σ_3 determined from the sum peak γ_{Σ_3} is finally compared with that derived from the angular distributions of the 2319-keV γ transition depopulating the third (5^-) excited state of ^{90}Zr in the bottom panel (c) of Fig. 7. In all cases the agreement is very good.

TABLE III. Same as Table II but for the $^{123}\text{Sb}(p, \gamma)^{124}\text{Te}$ reaction.

$E_{\text{c.m.}}$ (MeV)	σ_T (μb)	S factor (10^3 MeV b)	f_s
2.383	0.15 ± 0.05	$55\,970 \pm 18\,660$	1.104
2.583	0.60 ± 0.10	$66\,740 \pm 11\,120$	1.091
2.783	1.20 ± 0.15	$45\,580 \pm 5698$	1.081
2.983	2.45 ± 0.20	$35\,560 \pm 2903$	1.072
3.183	5.35 ± 0.35	$32\,600 \pm 2133$	1.065
3.383	8.70 ± 0.45	$24\,120 \pm 1247$	1.059

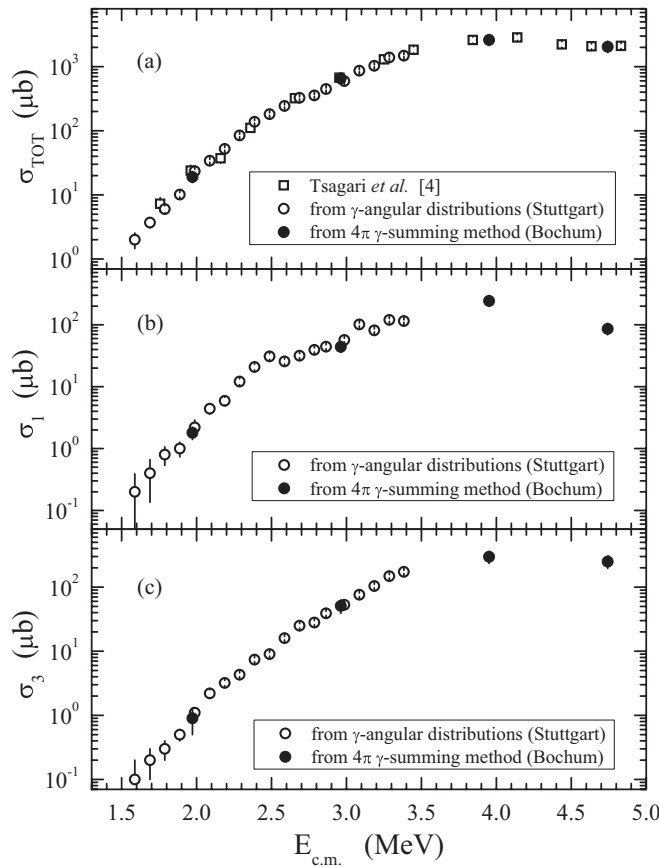


FIG. 7. Screening-corrected cross sections for the $^{89}\text{Y}(p, \gamma)^{90}\text{Zr}$ reaction from [4] (open squares), γ -angular distribution measurements (open circles), and the 4π γ -summing method (solid circles). The total cross sections are compared in the top panel. The cross sections σ_1 and σ_3 for the production of ^{90}Zr and subsequent decay to its first and third excited states, respectively, are plotted in the middle and the bottom panels.

IV. DISCUSSION

Proton capture reactions occurring at energies up to several MeV proceed through the formation and decay of a compound nucleus system provided that the nucleon separation energy is sufficiently high. The cross section for the decay of the compound nucleus into an open channel is given by the HF compound nucleus theory [1]. Essentially, it depends on the transmission coefficients for the formation of the compound nucleus and its decay into all the open channels (see, e.g., Ref. [10] for the formulas). When the compound nucleus is excited to states in the continuum, the transmission coefficients are averaged over spin and energy using an appropriate level density.

In this section, we compare our new data with HF cross sections calculated with the nuclear-reaction code TALYS 1.2 [19]. The code uses state-of-the-art nuclear reaction models and an updated nuclear structure data library [20] to calculate reaction cross sections in the energy range from 1 keV to 200 MeV. Information on ground-state properties, such as masses, deformations, and matter densities, are obtained from experimental data or from appropriate models of the

nuclear ground state. The properties of the excited states are obtained from experimental data and from NLD models. The particle transmission coefficients are determined by solving the nucleon-nucleus scattering problem with an appropriate OP for the particle-nucleus interaction. The photon transmission coefficients, however, are calculated assuming the dominance of dipole $E1/M1$ transitions. The γ -ray strength functions (γ SF) are directly related to the ground-state photoabsorption strength function for each excited state.

Different models, phenomenological or microscopic, global or local, exist for all these nuclear ingredients, and many of them are offered as options in TALYS 1.2 [19]. The sensitivity of low-energy proton-capture reaction cross sections to these models has been the subject of several studies involving medium and heavy nuclei at energies relevant to the p process [4,5,10,12,21] (see also Ref. [22] for a review). In this paper, we extend this systematic study to proton-capture reactions on ^{89}Y and $^{121,123}\text{Sb}$. For this purpose, we have used two global OPs available in TALYS: the default global phenomenological OP of Koning and Delaroche [23] (KD) and the global semimicroscopic Lane-consistent OP of Bauge, Delaroche, and Girod [24] (BDG). The latter is based on the microscopic OP of Jeukenne, Lejeune, and Mahaux [25], which has been extended to energies ranging from 1 keV to 200 MeV and has been compared with an extended database of nuclear data in that energy range. Furthermore, it makes exclusive use of the improved local density approximation (iLDA) to convert a nonlocal, infinite nuclear matter OP to a local OP for a finite nucleus. The nuclear matter densities used in the iLDA are obtained from Hartree-Fock-Bogoliubov calculations using either the Gogny or the Skyrme force. For NLDs, we have employed the constant-temperature Fermi-gas model NLDs (CTFG) specific to TALYS [19] and two microscopic models, namely the statistical Hartree-Fock-BCS NLDs of Demetriou and Goriely [26] (HFBCS) and the combinatorial microscopic NLDs of Hilaire and Goriely [27] (HG) based on the Hartree-Fock-Bogoliubov model (HFBCom). The CTFG NLDs are determined by combining the constant-temperature formula at low temperatures with the Fermi-gas model at higher temperatures where it is valid. The empirical formulas describing the single-particle level density a and the spin cutoff parameter σ^2 include shell corrections, energy dependence, and pairing effects and are adjusted globally to the bulk of existing data on low-lying excited states and s -wave neutron resonance spacings (see Ref. [19]). The microscopic HFBCS NLDs are calculated by applying the statistical method applied to the single-particle levels obtained from a Skyrme-Hartree-Fock model [26]. Pairing is treated within the BCS approach. Finally, the HFB NLDs are obtained by applying the combinatorial method to the single-particle level scheme produced by a Hartree-Fock-Bogoliubov model [27]. The HFBCS and HFBCom NLDs are also fitted to the available data on low-lying excited states and s -wave neutron resonance spacings.

For the γ -ray strength functions TALYS also includes several options. The GDR strength functions can be obtained either from the model of Kopecky and Uhl [28], who use a generalized Lorentzian form to describe the GDR shape with GDR parameters obtained from experiment where available,

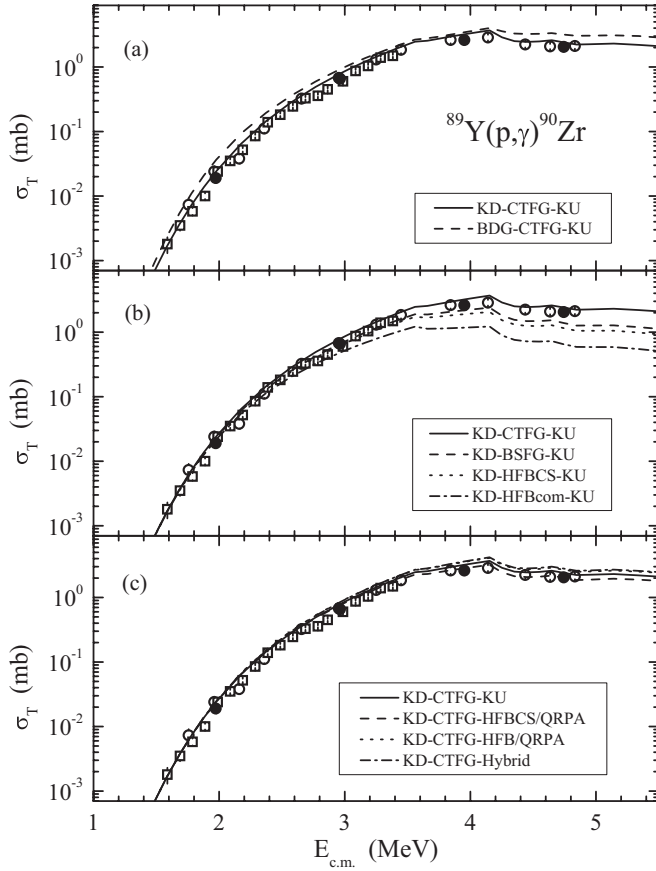


FIG. 8. The measured cross sections (circles and boxes) of the $^{89}\text{Y}(p, \gamma)^{90}\text{Zr}$ reaction are compared with TALYS calculations (curves) using two different OPs (top panel), different NLDs (middle panel), and different γ SFs (bottom panel). See text for more details.

or from systematics otherwise [20]. Alternatively, they can be determined by a microscopic model, whereby a Hartree-Fock-BCS or Hartree-Fock-Bogoliubov model describing the ground-state properties of the nucleus, is coupled with a quasi-random-phased-approximation (QRPA) method describing the excitation modes of the nucleus as phonon excitations. TALYS has incorporated two such models, namely, the HFBCS/QRPA [29] and the HFB/QRPA calculations [20,29]. It is expected that the former empirical model of Kopecky and Uhl will give satisfactory results at energies around the resonance energy, but would be unable to predict the $E1$ strength at energies below the neutron separation energy, where the microscopic models should be able to give more reliable predictions. The hybrid model of Goriely [30], based on a generalized Lorentzian with temperature dependence, was developed to deal with such inadequacies and is also implemented in TALYS.

In Figs. 8–10 the sensitivity of the cross sections to the three nuclear ingredients of the HF cross section formula, namely OP, NLDs, and γ SF, is shown separately for each ingredient, respectively. As can be seen from the figures, the cross sections are sensitive to all three ingredients when the neutron channel is open. This is clearly evident in the case of $^{89}\text{Y}(p, \gamma)^{90}\text{Zr}$ (Fig. 8), where the neutron channel opens at the energy of 2.4 MeV. Below the latter energy threshold the cross sections

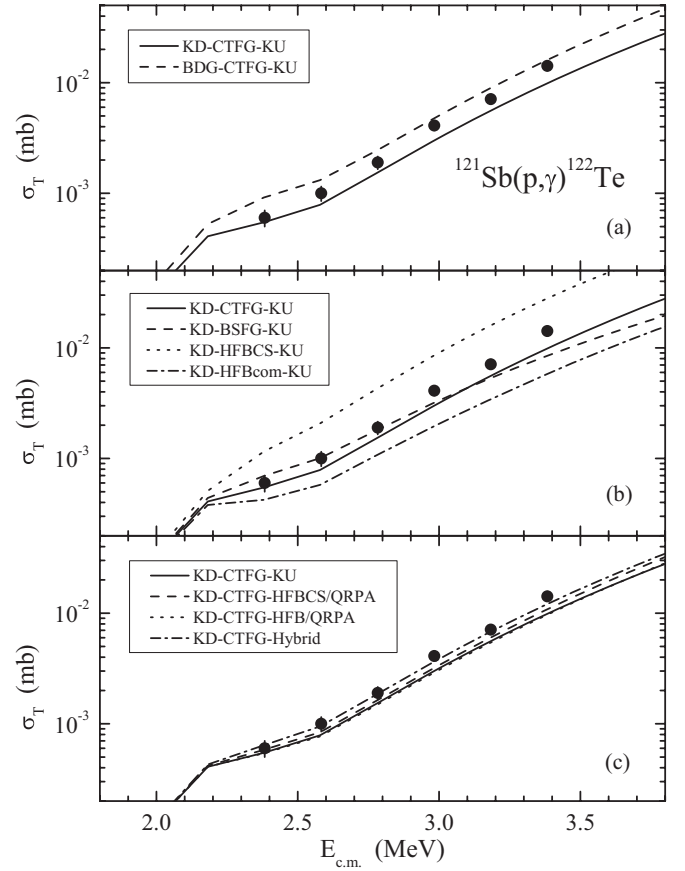


FIG. 9. Same as in Fig. 8 but for the $^{121}\text{Sb}(p, \gamma)^{122}\text{Te}$ reaction. See text for more details.

are only sensitive to the nucleon OP in the incident channel, while above that threshold they are also sensitive to the NLDs and γ SFs. Overall, one observes a larger scatter in the cross sections obtained from different NLD models (middle panel of Fig. 8), than in those obtained from different OPs and γ SF models. The results thus imply that the NLD models suffer from larger uncertainties compared to the nucleon OP and γ SFs.

All the combinations of the various models of the nuclear ingredients entering the HF formula that are included in TALYS, were used to obtain proton-capture excitation functions in the energy range covered by the present measurements. The different combinations yield largely varying cross sections reflecting the range of the uncertainties of the nuclear models used. To avoid overloaded figures, in Figs. 11 and 12 these uncertainties are shown by the shaded areas covering the area formed by the minimum and maximum calculated cross sections. The three curves plotted in the above figures correspond to three combinations of ingredients that are either phenomenological or microscopic and are as self-consistent as possible. These three combinations are labeled as TALYS-1, which includes the KD OP, CTFG NLDs, and KU γ SF; TALYS-2, including the BDG OP, HFBCS NLDs, and HFBCS/QRPA γ SF; and TALYS-3, including the BDG OP, HFBcom NLDs, and HFB/QRPA γ SFs. The aforementioned combinations do not necessarily provide the best agreement

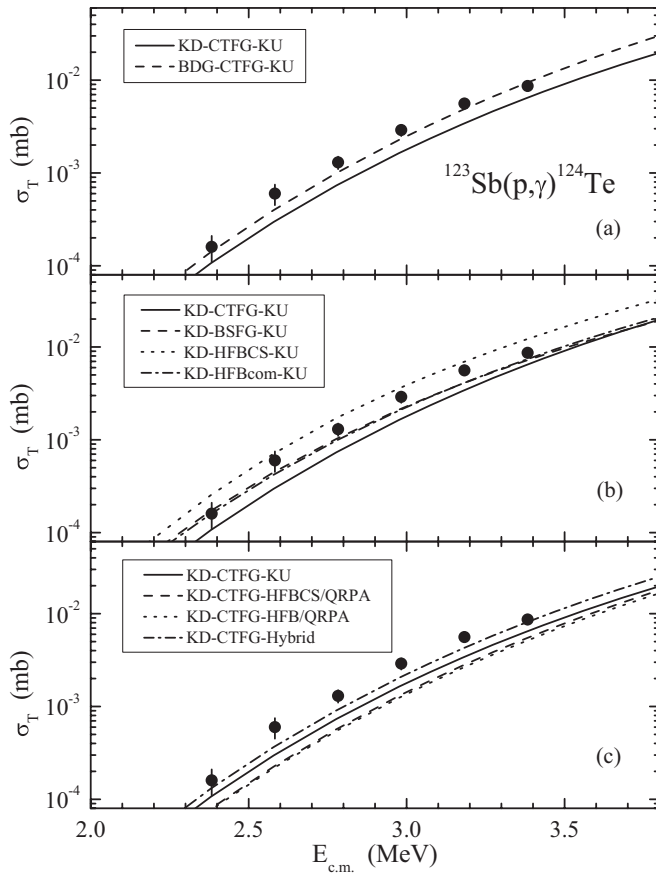


FIG. 10. Same as in Fig. 8 but for the $^{123}\text{Sb}(p, \gamma)^{124}\text{Te}$ reaction. See text for more details.

with the data; however, they are self-consistent in the sense that they combine only phenomenological or microscopic models, respectively. In the case of TALYS-2 and TALYS-3, in particular, the NLDs and γ SFs are obtained from the same microscopic models that are used to describe the ground-state properties of the nucleus. However, TALYS-1 is the default combination of input parameters in the TALYS code and as such is widely used in numerous applications so it is important to see how it performs in the case of low-lying proton-capture reactions as well. Also included in Figs. 11 and 12 are the (p, n) channel cross sections for further insight into the effect of the opening of the dominating neutron emission channel. The experimental (p, n) cross sections for $^{89}\text{Y}(p, n)^{90}\text{Zr}$ displayed in Fig. 11 were reported by Johnson *et al.* [31] and Mustafa *et al.* [32], whereas those plotted in Fig. 12 for $^{121}\text{Sb}(p, n)^{121}\text{Te}$ and $^{123}\text{Sb}(p, n)^{123}\text{Te}$ stem from the work of Batij *et al.* [33] and were obtained from the EXFOR database [34]. These experimental (p, n) cross sections are also compared with the corresponding TALYS-1, TALYS-2, and TALYS-3 predictions. As can be seen from the plots, in the case of ^{89}Y there is an energy region extending from 3.6 to 5.2 MeV where data for both the (p, γ) and (p, n) channels exist. The model calculations should be able to consistently describe both sets of data in this overlapping energy region. From the comparison, it is clear that TALYS-2 and TALYS-3 calculations underestimate the (p, γ) data while, as one would expect, they overestimate

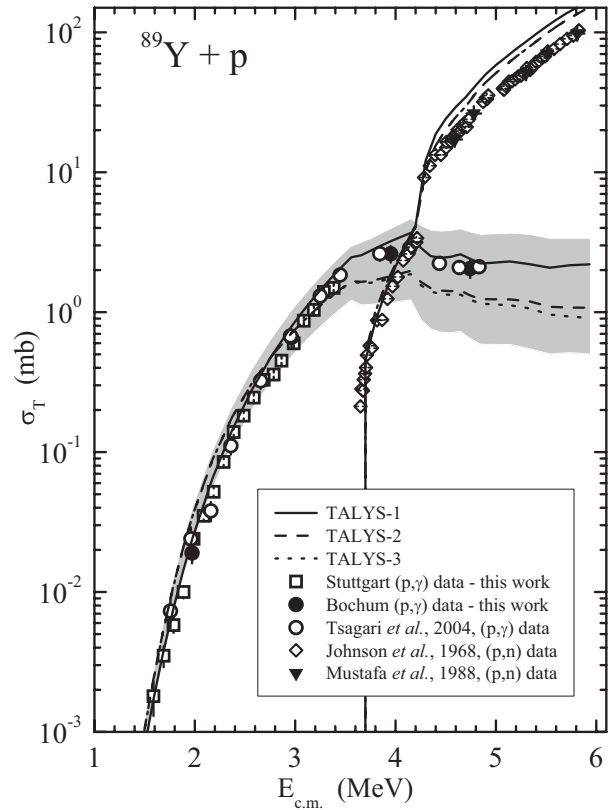


FIG. 11. Comparison of the measured cross sections (circles and boxes) of the $^{89}\text{Y}(p, \gamma)^{90}\text{Zr}$ reaction with the three different TALYS calculations TALYS-1, TALYS-2, TALYS-3 (curves) (see text for details). Also plotted are the cross sections for the (p, n) channel reported in Refs. [31,32].

the (p, n) data. However, TALYS-1 gives an overestimation of the (p, n) and to a lesser extent of the (p, γ) channel at the same time, implying that it may overestimate the other open reaction channels that are not included in the figure. From the comparison of all three nuclear targets, it is also obvious that at high energies where the neutron emission channel is by far the dominant one the (p, n) cross sections are only sensitive to the nucleon OPs in the incident channel, as is expected from the HF formula. Consequently, TALYS-2 and TALYS-3 are identical and differ from TALYS-1 because of the different OPs used. From the figures, it is also evident that there is no single combination that can reproduce all three sets of (p, γ) data. TALYS-1 describes the $^{89}\text{Y}(p, \gamma)^{90}\text{Zr}$ data best, but TALYS-3 gives the best agreement with the two other reaction data, $^{121}\text{Sb}(p, \gamma)^{122}\text{Te}$ and $^{123}\text{Sb}(p, \gamma)^{124}\text{Te}$. In the case of $^{89}\text{Y}(p, \gamma)^{90}\text{Zr}$, the BDG OP cannot reproduce the slope of the excitation function and leads to an overestimation of the data at low energies below the neutron threshold. TALYS-2 largely overestimates the $^{121}\text{Sb}(p, \gamma)^{122}\text{Te}$ data and somewhat less the $^{123}\text{Sb}(p, \gamma)^{124}\text{Te}$ data. TALYS-1, however, tends to slightly underestimate both these sets of data.

A. S factors

S factors are widely used in astrophysics applications for extrapolations to the very low energies of the astrophysically

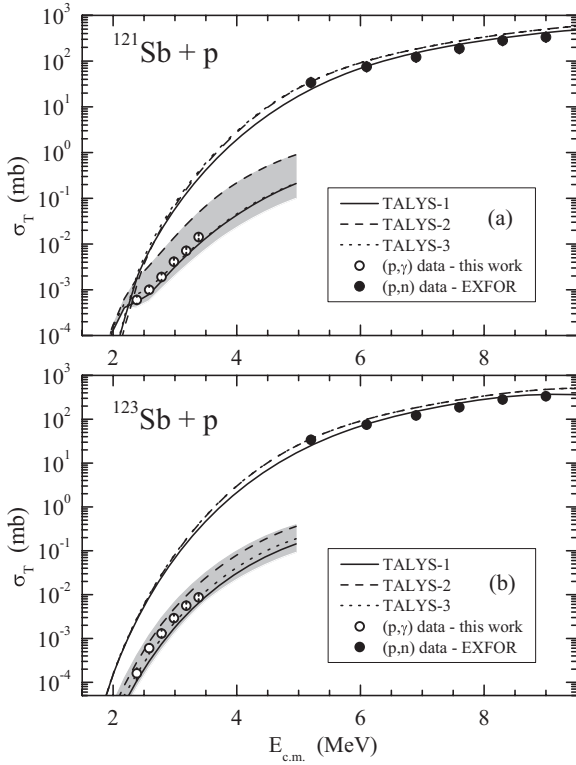


FIG. 12. Same as in Fig. 11 but for the $^{121}\text{Sb}(p, \gamma)^{122}\text{Te}$ (top panel) and $^{123}\text{Sb}(p, \gamma)^{124}\text{Te}$ (bottom panel) reactions (see text for details).

relevant Gamow window, where reaction cross sections cannot be measured. Having removed the Coulomb-dependent part of the cross section [see Eq. (9)], what is left (S) is a smoothly varying function of energy which allows for a more comprehensive comparison along the entire energy range and also for the aforementioned extrapolations. The S factors for the $^{89}\text{Y}(p, \gamma)^{90}\text{Zr}$, $^{121}\text{Sb}(p, \gamma)^{122}\text{Te}$, and $^{123}\text{Sb}(p, \gamma)^{124}\text{Te}$

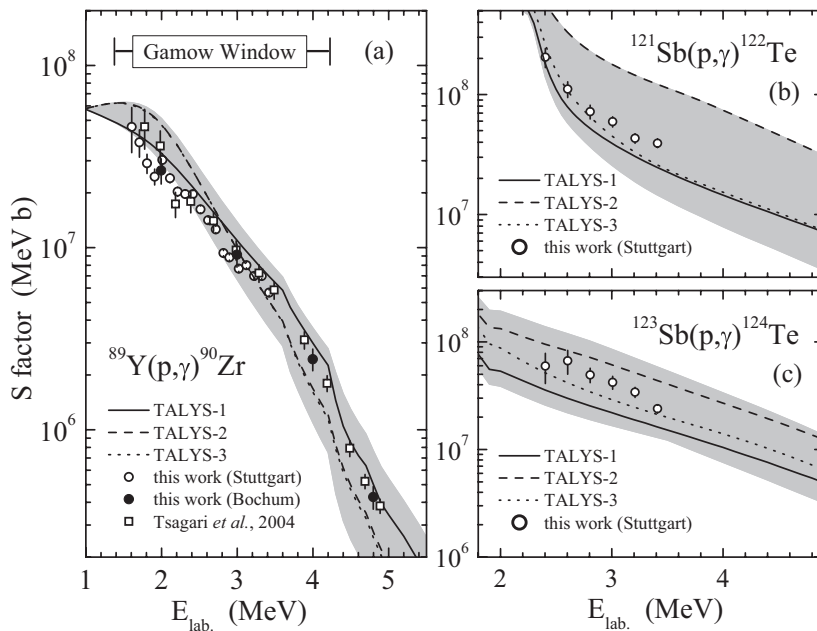


FIG. 13. Comparison of the measured astrophysical S factors (open or solid circles and open squares) of the (a) $^{89}\text{Y}(p, \gamma)^{90}\text{Zr}$, (b) $^{121}\text{Sb}(p, \gamma)^{122}\text{Te}$, and (c) $^{123}\text{Sb}(p, \gamma)^{124}\text{Te}$ reactions with the three different TALYS calculations (curves) TALYS-1, TALYS-2, and TALYS-3 (see text for details).

reactions are plotted in Fig. 13. Overall, all three combinations give a reasonable description of the data. However, a more detailed comparison shows that the experimental and theoretical S factors behave differently for the three reactions studied herein. In the case of ^{89}Y , TALYS-1 is the only combination with the correct energy dependence, which was not that obvious in the comparison between cross sections (see Fig. 11). However, TALYS-2 and TALYS-3 both overestimate the low-energy data and underestimate the higher-energy data. Because this is the only reaction where data have been measured at energies below the neutron threshold in this work, it is the only case where we can disentangle the effect of the nucleon OP from the NLDs and γSF . Thus, in the low-energy region below the neutron threshold, we can safely say that the proton OP KD [23] can describe the low-energy proton-induced data, whereas BDG [24] cannot. For the reactions on the ^{121}Sb and ^{123}Sb isotopes, the cross sections have been measured above the neutron threshold where all the nuclear ingredients, namely OPs, NLDs, and γSF s, associated with the competing channels can influence the cross section and, therefore, we cannot draw any conclusions on the nucleon OP. The shaded areas in Fig. 13 depict the range of uncertainties of the calculations owing to the poorly known nuclear ingredients and correspond to the shaded areas of Figs. 11 and 12.

B. Reaction rates

To evaluate the impact of the above-mentioned nuclear physics uncertainties on nucleosynthesis calculations, we compare the reaction rates resulting from the different combinations of nuclear ingredients at stellar temperatures relevant to the p -process nucleosynthesis. The latter is assumed to occur at temperatures ranging from 1.8×10^9 K to 3.3×10^9 K that are maintained for about 1 s.

In the case of ^{89}Y and $^{121,123}\text{Sb}$, this temperature range is equivalent to proton-beam energies from 1.3 to 4.2 MeV and 1.8 to 4.9 MeV, respectively. Our present measurements

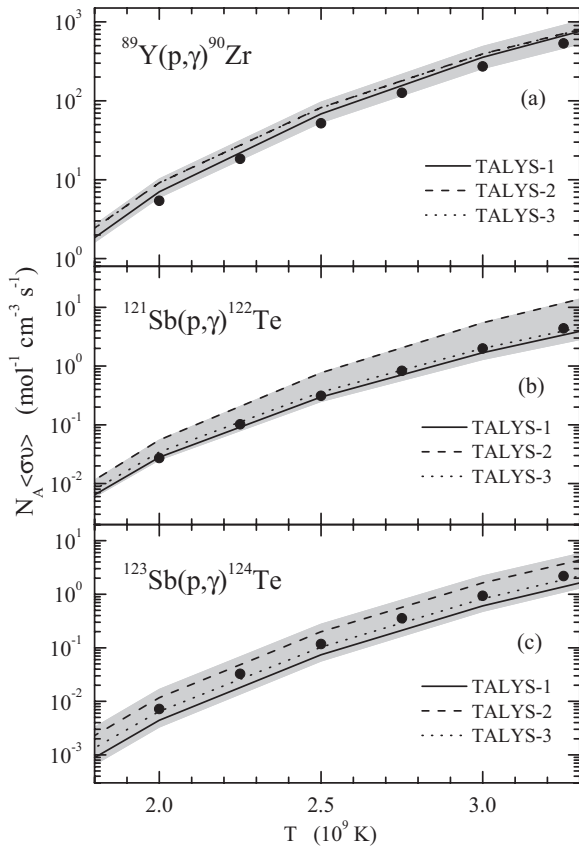


FIG. 14. Same as in Fig. 13 but for the ground-state RRs.

cover a good part of the Gamow energy window mentioned above. The ground-state reaction rates, $\langle\sigma v\rangle$, often referred to as laboratory reaction rates, are derived from the respective total cross sections σ_T for different temperatures T by

$$N_A \langle\sigma v\rangle = \left(\frac{8}{\pi\mu}\right)^{1/2} \frac{N_A}{(kT)^{3/2}} \times \int_0^\infty \sigma_T(E) \cdot E \cdot \exp\left(-\frac{E}{kT}\right) dE, \quad (10)$$

where N_A is the Avogadro's number, μ is the reduced mass, kT is the thermal energy, and E is the center-of-mass energy.

The reaction rates resulting from the different TALYS combinations mentioned in the previous sections are shown in Fig. 14 for temperatures relevant to the p process. The shaded area is formed by the reaction rates obtained with all possible combinations of nuclear parameters available in TALYS and corresponds to the shaded areas in the cross section plots in Figs. 11–13. The reaction rates obtained with TALYS-1, TALYS-2, and TALYS-3 are also plotted (solid, dashed, and dotted lines, respectively). In the previous sections we established that TALYS-1, and TALYS-3 give the best description of the measured cross sections for the $^{89}\text{Y}(p, \gamma)^{90}\text{Zr}$ and $^{121,123}\text{Sb}(p, \gamma)^{122,124}\text{Te}$ reactions, respectively. The corresponding reaction rates, RRs, are also expected to be the best set of ground-state rates for the ^{89}Y and $^{121,123}\text{Sb}$ isotopes. For further illustration, in Fig. 15 we plot the ratios r_{RR} of the highest and lowest RRs obtained with TALYS—which

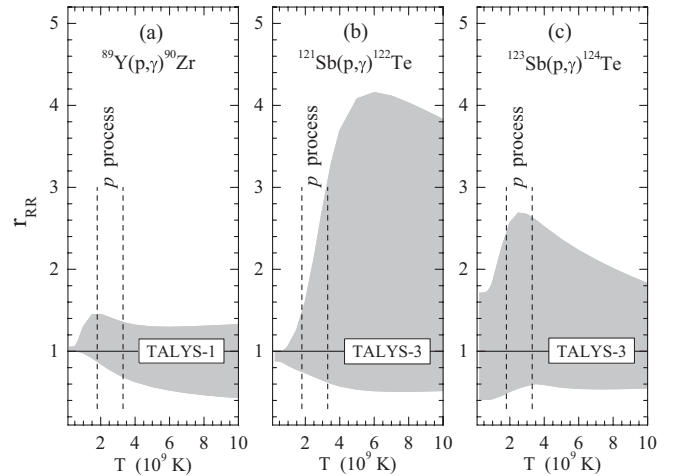


FIG. 15. Ratios of the upper and lower calculated RRs over the best combination TALYS-1 for the $^{89}\text{Y}(p, \gamma)^{90}\text{Zr}$ reaction (left panel), TALYS-3 for the reaction $^{121}\text{Sb}(p, \gamma)^{122}\text{Te}$ (middle panel), and TALYS-3 for the $^{123}\text{Sb}(p, \gamma)^{124}\text{Te}$ (right panel) (see text for details).

also determine the borders of the shaded areas—over these best rates, as a function of temperature T for temperatures ranging from 1×10^9 K to 10×10^9 K. Clearly, from the figure one can see that, for all the nuclei studied herein, the uncertainties in the ground-state rates arising from the uncertainties in the HF calculations are limited within a factor of 3 for temperatures relevant to the p process. Thus, the nuclear uncertainties are well contained within the range of uncertainties in the reproduction of the p -nuclei abundances by the various p -process models.

C. Isomeric cross section ratios

In addition to measuring the total cross sections for the proton-capture reactions, for the $^{89}\text{Y}(p, \gamma)^{90}\text{Zr}$ reaction, it was also possible to determine the cross sections for the formation of ^{90}Zr in the ground 0^+ and two metastable states 0^+ at $E = 1.761$ MeV, and 5^- at $E = 2.319$ MeV, respectively. The ratios of the metastable to the ground-state cross section, i.e., σ_{1761}/σ_0 and σ_{2319}/σ_0 , commonly referred to as isomeric cross section ratios, are compared with the TALYS-1, TALYS-2, and TALYS-3 results in Fig. 16. Isomeric cross section ratios are particularly useful in understanding the transfer of angular momentum in nuclear reactions and checking nuclear reaction model parameters. Because isomeric ratios probe the spin dependence of the nuclear reactions, the comparison between the calculated isomeric ratios boils down to a comparison between the spin-dependent part of the corresponding NLDs, namely the CTFG, HFBCS, and HFBcom NLDs. Of the three NLDs, CTFG, and HFBCS adopt a Gaussian-type spin dependence with parameters adjusted to data, while HFBcom is based on a combinatorial approach that is also applied to the spin and parity of the single-particle states, and therefore is expected to be more realistic and reliable. From Fig. 16, we see that the results from the three combinations TALYS-1, TALYS-2, and TALYS-3 do not differ significantly and overall reproduce the trend of the isomeric ratios. TALYS-2 and TALYS-3

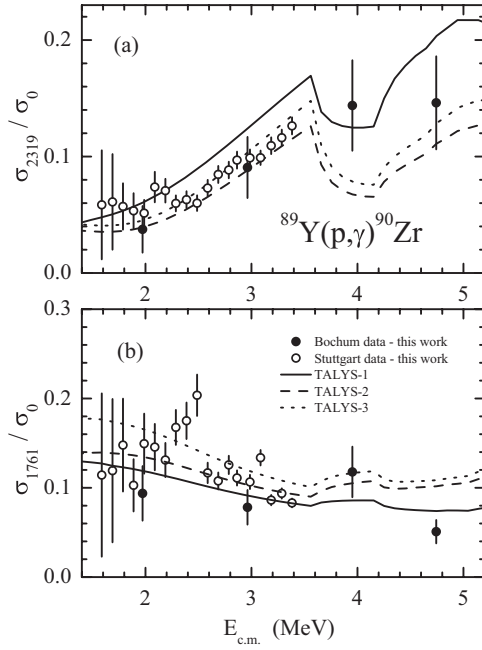


FIG. 16. Comparison of the isomeric cross section ratios σ_{1761}/σ_0 and σ_{2319}/σ_0 (circles) of the $^{89}\text{Y}(p, \gamma)^{90}\text{Zr}$ with the three different TALYS calculations (curves) TALYS-1, TALYS-2, TALYS-3 (see text for details).

are in very close agreement while the differences with TALYS-1 are more evident in σ_{2319}/σ_0 . Similarly, when comparing the isomeric ratio $\sigma_g/(\sigma_g + \sigma_m)$ for the $^{89}\text{Y}(p, n)^{89}\text{Zr}$ reaction [35] (see Fig. 17) one can see that all three combinations agree with the data. For completeness, in Fig. 18 we show a comparison between experimental [33,34] and calculated isomeric ratios for the $^{121}\text{Sb}(p, n)^{121}\text{Te}$ and $^{123}\text{Sb}(p, n)^{123}\text{Te}$ reactions as well. In the latter cases, the spin parametrization of the CTFG model seems to describe the data far better than the one of the HFBCS and HFBCOM model, which tend to overestimate the experimental ratios. These results are somewhat reassuring for the CTFG and HFBCS models, as they demonstrate that although these models are phenomenological as far as the

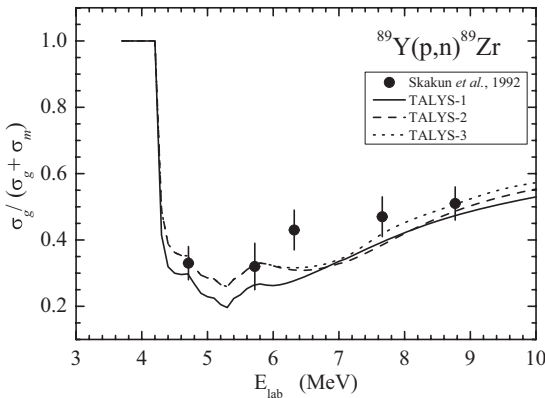


FIG. 17. Comparison of the isomeric cross section ratio $\sigma_m/(\sigma_g + \sigma_m)$ (circles) of the $^{89}\text{Y}(p, n)^{89}\text{Zr}$ reaction [35] with the three different TALYS calculations (curves) TALYS-1, TALYS-2, TALYS-3 (see text for details).

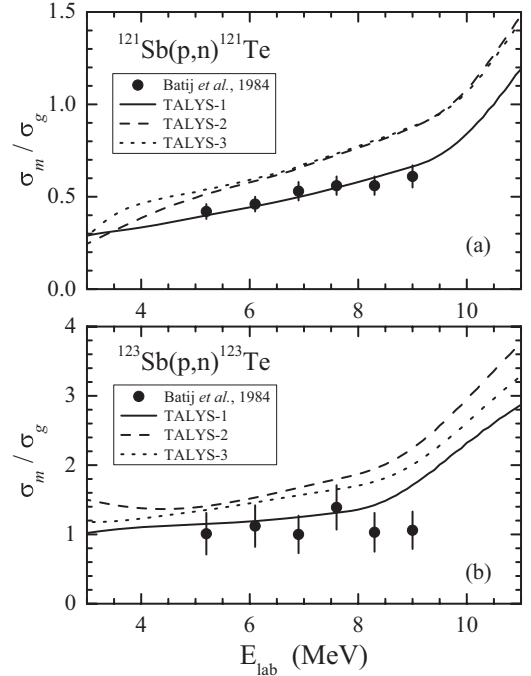


FIG. 18. Comparison of the isomeric cross section ratio σ_m/σ_g (circles) of the $^{121}\text{Sb}(p, n)^{121}\text{Te}$ and $^{123}\text{Sb}(p, n)^{123}\text{Te}$ reactions [33,34] with the three different TALYS calculations (curves) TALYS-1, TALYS-2, TALYS-3 (see text for details).

spin distribution is concerned, they give reasonable results that agree with the more accurate combinatorial method and in some cases are even better.

V. CONCLUSIONS

The total cross sections for proton capture reactions on ^{89}Y , ^{121}Sb , and ^{123}Sb were measured at beam energies ranging from 1.6 to 4.8 MeV. The measured cross sections were compared with the HF calculations using the nuclear reaction code TALYS [19]. The most updated nuclear structure libraries [20] have been used to calculate the nuclear ingredients of the HF model.

Several global microscopic and phenomenological models of optical potentials, NLDs, and γ -ray strength functions have been tested. The results show that in the low-energy region of interest, proton-capture cross sections are more sensitive to the uncertainties related to the NLDs than to the other ingredients, such as the nucleon-nucleus OP and the γ SF. There is no single combination of nuclear models that can reproduce all three data sets equally well. It was thus decided that three combinations of nuclear input should be investigated in more detail: a purely phenomenological one (TALYS-1) and two semimicroscopic ones (TALYS-2 and TALYS-3) that use the same microscopic model for the ground-state, excited-state, and photoabsorption properties of the nucleus and hence are self-consistent. The results show that TALYS-1 describes the $^{89}\text{Y}(p, \gamma)^{90}\text{Zr}$ data well, while TALYS-3 describes the $^{121}\text{Sb}(p, \gamma)^{122}\text{Te}$ and $^{123}\text{Sb}(p, \gamma)^{124}\text{Te}$ data fairly well. TALYS-2 agrees with TALYS-3 for ^{89}Y but it tends to overestimate the data for $^{121,123}\text{Sb}$. The astrophysical S factors

and RRs resulting from the TALYS-1, TALYS-2, and TALYS-3 cross sections were also compared with the experimental data. In the case of $^{89}\text{Y}(p, \gamma)^{90}\text{Zr}$, the proton OP of Koning and Delaroche [23] is able to reproduce the energy dependence of the excitation function and S factor while the OP of Bauge *et al.* [24] is not. The effect of the different combinations on the ground-state RRs was also studied and the uncertainties arising from the HF calculations were shown to be less than a factor of 3, which is well below the average discrepancies observed between calculated p -nuclei abundances and observations. Furthermore, our results show that combinations of global microscopic models of nuclear ingredients are able to perform equally well as phenomenological global models and in some cases even better. Finally, isomeric cross section ratios were also determined for the $^{89}\text{Y}(p, \gamma)^{90}\text{Zr}$ reaction and were compared with TALYS-1, TALYS-2, and TALYS-3 results. Overall, reasonable agreement was found between data and model calculations, implying that the spin-dependent terms of the

NLDs are reliable. For completeness, we have also compared isomeric ratios for the corresponding (p, n) channels; however, in this case the phenomenological combination TALYS-1 is the only one able to describe all the data for ^{89}Y as well as for $^{121,123}\text{Sb}$ nuclei.

To summarize, we have shown that it is extremely useful to perform systematic studies of proton-capture reactions in this energy and mass region, as it enables us to assess the validity of the models used for determining the HF nuclear ingredients and thus make improvements that would further reduce the associated uncertainties.

ACKNOWLEDGMENTS

This work was supported by the Hellenic State Scholarship Foundation (IKY) and the German Academic Exchange Service (DAAD) within the IKYDA2002 funding program as well as the FP7/REGPOT/LIBRA project (Grant No. 230123).

-
- [1] W. Hauser and H. Feshbach, *Phys. Rev.* **87**, 366 (1952).
 [2] M. Arnould and S. Goriely, *Phys. Rep.* **384**, 1 (2003).
 [3] A. Spyrou, H.-W. Becker, A. Lagoyannis, S. Harissopulos, and C. Rolfs, *Phys. Rev. C* **76**, 015802 (2007).
 [4] P. Tsagari, M. Kokkoris, E. Skreti, A. G. Karydas, S. Harissopulos, T. Paradellis, and P. Demetriou, *Phys. Rev. C* **70**, 015802 (2004).
 [5] S. Galanopoulos, P. Demetriou, M. Kokkoris, S. Harissopulos, R. Kunz, M. Fey, J. W. Hammer, Gy. Gyürky, Zs. Fülop, E. Somorjai, and S. Goriely, *Phys. Rev. C* **67**, 015801 (2003).
 [6] A. Anttila, J. Keinonen, M. Hautala, and I. Forsblom, *Nucl. Instrum. Methods* **147**, 501 (1977).
 [7] P. M. Endt, C. Alderliesten, F. Zijderhand, A. A. Wolters, and A. G. M. Van Hees, *Nucl. Phys. A* **510**, 209 (1990).
 [8] K. Debertin and R. G. Helmer, *Gamma- and X-ray Spectrometry with Semiconductor Detectors* (North-Holland, Elsevier Science, Amsterdam, 1988).
 [9] R. B. Firestone, V. S. Shirley, C. M. Baglin, J. Zipkin, and S. Y. F. Chu, *Table of Isotopes*, 8th ed. (Wiley-Interscience, New York, 1996).
 [10] A. Spyrou, A. Lagoyannis, P. Demetriou, S. Harissopulos, and H.-W. Becker, *Phys. Rev. C* **77**, 065801 (2008).
 [11] S. Harissopulos, C. Chronidou, K. Spyrou, S. Kossionides, T. Paradellis, C. Rolfs, W. H. Schulte, and H. W. Becker, *Eur. Phys. J. A* **9**, 479 (2000).
 [12] S. Harissopulos, E. Skreti, P. Tsagari, G. Souliotis, P. Demetriou, T. Paradellis, J. W. Hammer, R. Kunz, C. Angulo, S. Goriely, and T. Rauscher, *Phys. Rev. C* **64**, 055804 (2001).
 [13] D. C. Camp and A. L. Van Lehn, *Nucl. Instrum. Methods* **76**, 192 (1969).
 [14] S. Agostinelli *et al.*, *Nucl. Instrum. Methods A* **506**, 250 (2003).
 [15] J. F. Ziegler and J. P. Biersack, Code SRIM version 2003; full description given by J. F. Ziegler, J. P. Biersack, and U. Littmark, *The Stopping and Range of Ions in Solids* (Pergamon, New York, 1985).
 [16] C. E. Rolfs and W. S. Rodney, *Cauldrons in the Cosmos* (The University of Chicago Press, Chicago, 1988).
 [17] C. E. Rolfs, *Nucl. Phys. News* **16**, 9 (2006); (private communication).
 [18] K. U. Kettner, H. W. Becker, F. Strieder, and C. Rolfs, *J. Phys. G* **32**, 489 (2006).
 [19] A. J. Koning, S. Hilaire, and M. C. Duijvestijn, in *Proceedings of the International Conference on Nuclear Data for Science and Technology, Nice, France, 2007*, edited by O. Bersillon, F. Gunsing, E. Bauge, R. Jacqmin, and S. Leray (EDP Sciences, Les Ulis, France, 2008), p. 211 (available online at <http://dx.doi.org/10.1051/ndata:07767>).
 [20] R. Capote *et al.*, *Nucl. Data Sheets* **110**, 3107 (2009).
 [21] S. Harissopulos, A. Lagoyannis, A. Spyrou, Ch. Zarkadas, S. Galanopoulos, G. Perdikakis, H.-W. Becker, C. Rolfs, F. Strieder, R. Kunz, M. Fey, J. W. Hammer, A. Dewald, K.-O. Zell, P. von Brentato, R. Julin, and P. Demetriou, *J. Phys. G* **31**, S1417 (2005).
 [22] M. Arnould and S. Goriely, *Nucl. Phys. A* **777**, 157 (2006).
 [23] A. J. Koning and J. P. Delaroche, *Nucl. Phys. A* **713**, 231 (2003).
 [24] E. Bauge, J. P. Delaroche, and M. Girod, *Phys. Rev. C* **63**, 024607 (2001).
 [25] J. P. Jeukenne, A. Lejeune, and C. Mahaux, *Phys. Rev. C* **16**, 80 (1977).
 [26] P. Demetriou and S. Goriely, *Nucl. Phys. A* **695**, 95 (2001).
 [27] S. Goriely, S. Hilaire, and A. J. Koning, *Phys. Rev. C* **78**, 064307 (2008).
 [28] J. Kopecky and M. Uhl, *Phys. Rev. C* **41**, 1941 (1990).
 [29] E. Khan, S. Goriely, D. Allard, E. Parizot, T. Suomijarvi, A. J. Koning, S. Hilaire, and M. C. Duijvestijn, *Astropart. Phys.* **23**, 191 (2005).
 [30] S. Goriely, *Phys. Lett. B* **436**, 10 (1998).
 [31] C. H. Johnson, R. L. Kernell, and S. Ramavataram, *Nucl. Phys. A* **107**, 21 (1968).
 [32] M. G. Mustafa, H. I. West, H. O'Brien, R. G. Lanier, M. Benhamou, and T. Tamura, *Phys. Rev. C* **38**, 1624 (1988).
 [33] V. G. Batij, E. A. Skakun, O. A. Rastrepin, and Ju. N. Rakivnenko, *Izv. Akad. Nauk SSSR, Ser. Fiz.* **48**, 194 (1984).
 [34] EXFOR Experimental Nuclear Reaction Data, <http://www-nds.iaea.org/exfor/exfor.htm>.
 [35] E. A. Skakun and V. G. Batij, *Z. Phys. A* **344**, 13 (1992).